

Computational Analysis of Structure-Activity Relationships in Highly Active Homogeneous Ruthenium—Based Water **Oxidation Catalysts**

Gabriel Bury D and Yulia Pushkar *

Department of Physics and Astronomy, Purdue University, West Lafayette, IN 47907, USA * Correspondence: ypushkar@purdue.edu

Abstract: Linear free—energy scaling relationships (LFESRs) and regression analysis may predict the catalytic performance of heterogeneous and recently, homogenous water oxidation catalysts (WOCs). This study analyses thirteen homogeneous Ru-based catalysts—some, the most active catalysts studied: the Ru(tpy-R)(QC) and Ru(tpy-R)(4-pic)₂ complexes, where tpy is 2,2';6',2"-terpyridine, QC is 8-quinolinecarboxylate and 4-pic is 4-picoline. Typical relationships studied among heterogenous catalysts cannot be applied to homogeneous catalysts. The selected group of structurally similar catalysts with impressive catalytic activity deserves closer computational and statistical analysis of multiple reaction step energetics correlating with measured catalytic activity. We report general methods of LFESR analysis yield insufficiently robust relationships between descriptor variables. However, volcano-plot-based analysis grounded in Sabatier's principle reveals ideal relative energies of the $Ru^{IV} = O$ and $Ru^{IV} - OH$ intermediates and optimal changes in free energies of water nucleophilic attack on Ru^V = O. A narrow range of Ru^{IV} – OH to Ru^V = O redox potentials corresponding with the highest catalytic activities suggests facile access to the catalytically competent high-valent RuV = O state, often inaccessible from Ru^{IV} = O. Our work incorporates experimental oxygen evolution rates into approaches of LFESR and Sabatier-principle-based analysis, identifying a narrow yet fertile energetic landscape to bountiful oxygen evolution activity, leading to future rational design.

Keywords: density functional theory; water oxidation; homogeneous catalysis; reactive intermediates; ruthenium; volcano plot; scaling relationships; Sabatier principle; Gibbs free energy

1. Introduction

The harvesting of sunlight offers a gateway into a sustainable energy future by providing a clean means to satiate the world's growing hunger for energy while providing a solution to the developing global climate change concerns [1]. The current challenge is in the harvesting and utilization of solar energy efficiently. The generation of solar fuels via artificial photosynthetic processes is an attractive method for harvesting this sunlight [2–6]. Numerous conceptual schemes have been proposed in which sunlight drives the flow of electrons and generation of protons, leading to O-O bond formation and the evolution of molecular oxygen, O_2 ; the coupling of this proton and electron movement to water oxidation catalysts (WOCs) facilitates the breaking of bonds in water with formation of H₂ and O₂ [7,8]. The most significant bottleneck in the light-driven water splitting is the oxygen—evolving reaction (OER) [9]:

$$2H_2O \rightarrow O_2 + 4H^+ + 4e^-$$
 (E⁰ = 1.23 V versus NHE at pH 0). (1)

Current catalysts do not satisfy the need for cost efficiency, activity, and stability for this endergonic reaction; currently available catalysts suffer from limited catalytic activity due to significant overpotentials (\geq 400 mV). As such, research into the development and



Citation: Bury, G.; Pushkar, Y. Computational Analysis of Structure-Activity Relationships in Highly Active Homogeneous Ruthenium-Based Water Oxidation Catalysts. Catalysts 2022, 12, 863. https://doi.org/10.3390/ catal12080863

Academic Editor: Lan Chen

Received: 6 July 2022 Accepted: 28 July 2022 Published: 5 August 2022

Publisher's Note: MDPI stays neutral with regard to jurisdictional claims in published maps and institutional affil-



Copyright: © 2022 by the authors. Licensee MDPI, Basel, Switzerland This article is an open access article distributed under the terms and conditions of the Creative Commons Attribution (CC BY) license (https:// creativecommons.org/licenses/by/ 4.0/).

Catalysts **2022**, 12, 863 2 of 15

design of sufficiently stable and efficient catalysts capable of facilitating solar—driven water oxidation has grown significantly in recent years [10–16].

Historically, many catalysts were discovered through trial and error via synthesis and experimentation, although a more sophisticated approach adopts the mentality of rational design-development and design of novel catalysts with consideration of known catalytic theory to increase the likelihood of synthesizing an effective catalyst [17,18]. If computational theory and modelling may be employed to study and successfully characterize candidate catalysts and predict their catalytic competence, significant time can be spared in synthesizing and experimentally characterizing ineffective options. With the rapid improvement in the speed and capabilities of computational software and technologies, such an approach is becoming very alluring. Work has been conducted in the computational characterization of broad ranges of catalytic families and systems [19–21]. Popular are scaling relationships, employed to describe metal-organic frameworks [22,23], single—atom catalysts [24,25], and other heterogenous [26,27] and homogenous [28–30] systems. These scaling relationships relate parameters of a catalyst or its mechanism with predictors of strong catalytic activity, either oxidation rate, (low) overpotentials, turnover frequencies, or reduced energetic barriers in key mechanistic steps. The use of linear scaling relationships serves to reduce some of the systemic error [31–33] inherent in some computational methods, such as density functional theory (DFT), which may differ in their treatment of static correlation and electron localization. Since scaling relationships predict the relative activity of the catalysts, these systemic errors prove less significant in most cases. Despite the demonstrated need [34] for specifically chosen scaling relationships in homogenous catalysis based on ligand motifs, recent proposals still describe universal [35] scaling relationships for WOCs. Such reports are absent for the Ru(NNN)(NN) – based and similarly structured family of catalysts, home to some very highly active OER catalysts. Our computational analysis includes numerous Ru(NNN)(NN)—based catalysts, as well as Ru(bda)(N)(N) and several Ru(NNN)(QC) catalysts—some of the most active for Ru–based water oxidation catalysis. The analyzed complexes contain neutral polypyridine ligands alongside negatively charged QC (-1) and bda (-2) ligands (Figure 1).

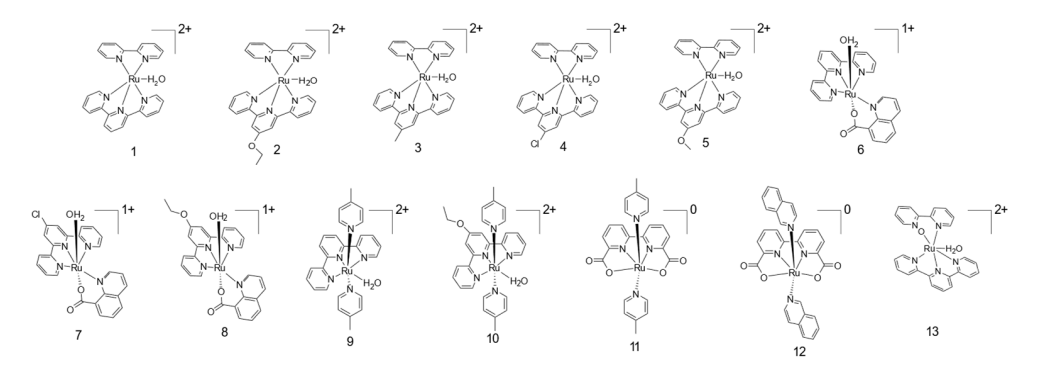


Figure 1. A schematic representation of the complexes considered in this study. (1) Ru(tpy)(bpy) (2) Ru(tpyEtO)(bpy) (3) Ru(tpyMe)(bpy) (4) Ru(tpy—Cl)(bpy) (5) Ru(tpyMeO)(bpy) (6) trans—Ru(tpy)(QC) (7) trans—Ru(tpy—Cl)(QC) (8) trans—Ru(EtOtpy)(QC) (9) Ru(tpy)(4—pic)₂ (10) Ru(EtOtpy)(4—pic)₂ (11) Ru(bda)(4—pic)₂ (12) Ru(bda)(isoq)₂ (13) Ru(tpy)(bpyNO).

The OER process occurs via a series of redox steps involving various reaction intermediates. The metal center coordinates water and is successively oxidized. Later, an O-O bond is formed, and molecular oxygen is ultimately released. Two primary paths lead to O-O bonds: water nucleophilic attack (WNA) and the interaction of two metal—oxo moieties (I2M) [17,36,37]; below, Figure 2 outlines the possible redox reactions in a mechanism for a generic WOC, forming an O-O bond through a WNA process on the high—valent $Ru^V = O$ state. Ru—based WOCs will start in an initial Ru^{II} valent state, possibly coordinated by H_2O , although bda—type catalysts do not have water coordinated in the initial state. Following a series of possible redox reactions (right side of Figure 2), the catalyst

Catalysts **2022**, 12, 863 3 of 15

attains a high valent, catalytically competent state, at which point, WNA or I2M processes are not energetically inhibited. Most mononuclear Ru—based catalysts will undergo some redox processes shown in Figure 2 during their catalytic mechanism [38–40].

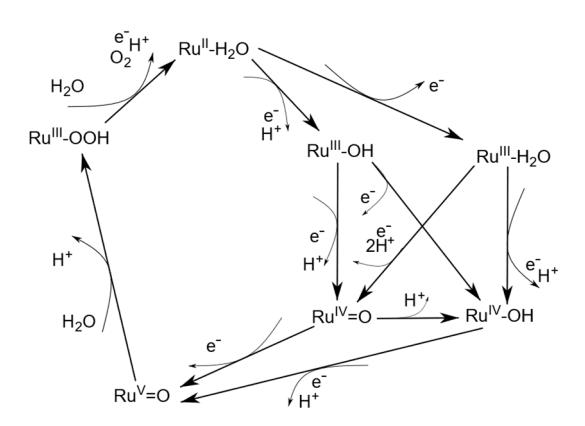


Figure 2. Possible pathways for oxidation and proton—coupled electron transfer of a WOC forming an O-O bond via water nucleophilic attack on the Ru V = O state.

Both methods of O-O bond formation are preceded by proton-coupled oxidation, which comprises three electron transfer events (ET) and two proton transfer events. Often, ET events are coupled to the transfer of a proton at the same time, in which case this proton-coupled electron transfer (PCET) allows for the reduction of energetic barriers during charge transfer. In the case of WNA, a Ru-oxo species is attacked by a solvent water molecule with a proton transfer, succeeded by further electron transfer prior to, or in concert with, the release of molecular oxygen (details of these later steps were not investigated); I2M mechanisms simply involve a coupling of two metal-oxo groups, resulting in the O-O bond requisite for O $_2$ evolution. A substantial history of work on Ru-based WOCs [39,41-44] suggests that both WNA and I2M processes occur more easily upon reaching the high-valent Ru V = O state. Such studies describe the catalytic cycles leading to O $_2$ evolution in roughly four steps, each characterized by the removal of one electron:

$$Ru^{II} - H_2O \rightarrow Ru^{III} - OH + H^+ + e^-$$
 (2)

$$Ru^{III} - OH \rightarrow Ru^{IV} = O + H^{+} + e^{-}$$
(3)

$$Ru^{IV} = O + H_2O \rightarrow Ru^{III} - OOH + H^+ + e^-$$
, and (4)

$$Ru^{III} - OOH \rightarrow Ru^{II} + O_2 + H^+ + e^-.$$
 (5)

From the relative Gibbs energies in the reactions above, changes in free energies for each reaction step, ΔG_i , lead to the determination of the most thermodynamically difficult step and, by extension, the theoretical overpotential η_{th} [17]:

$$\eta_{th} = \text{Max}[\Delta G_i] - 1.23 \text{ V}. \tag{6}$$

This implies that the ideal catalyst, with $\eta_{th}=0$, would have distributed overall change in free energy equally across each step in the reaction process; $\Delta G_i=1.23~V$ for all i. For most Ru-based catalysts, O-O bond formation from Ru^{IV} intermediates via WNA or I2M processes is difficult; access to the high-valent Ru^V = O intermediate lowers barriers sufficiently to allow for O-O bond formation. However, in many Ru-based WOCs, direct oxidation from Ru^{IV} = O to Ru^V = O occurs at high potentials ($\geq 1.7~V$) [44–46]. At the same time, some Ru-based WOCs boast very high rates of oxygen evolution. This suggests that the Ru^V = O state might be achievable in some WOCs. Figure 2 posits an alternate pathway to this single-electron oxidation step from Ru^{IV} = O. For Ru^{IV}-OH species produced either by an ET step from Ru^{III} or via protonation of the Ru^{IV} = O species, a PCET step at a much more accessible potential (~ 1.4 –1.6~V) can be driven by sacrificial oxidants such as

Catalysts **2022**, 12, 863 4 of 15

cerium(IV) ammonium nitrate (CAN) or electrochemically [47]. Numerous high—valent $Ru^V = O$ species of catalytically competent WOCs have been observed through the use of electron paramagnetic resonance (EPR) [45,48–51]. Ru^V EPR features are rhombic and have g—tensors near ($g_{xx} \sim 2.1$, $g_{yy} \sim 2.0$, $g_{zz} \sim 1.9$) [44], although one recent study reported a significantly different, highly anisotropic EPR signal assigned to Ru^V , [52] which we suggest is better described as a complex of Ru^{III} with a modified ligand.

Based on the known mechanisms of WOC action, we tailor the generalized conventions of LFESR analysis—broadly applied to heterogeneous and solid—state catalysts—to a subset of highly active, Ru—based, homogenous catalysts with Ru(NNN)(NN) or similar structures. The consideration of an additional ET/PCET event prior to O–O bond formation—necessary to yield the Ru $^{\rm V}$ states—is added in the analysis. These modifications reveal insights into the ideal range of relative energies of the Ru $^{\rm IV}$ = O and Ru $^{\rm IV}$ –OH intermediates, as well as a narrow region of optimal change in free energy of WNA on Ru $^{\rm V}$ reactions: ΔG ~>–0.1 eV. Finally, a narrow range of Ru $^{\rm IV}$ –OH to Ru $^{\rm V}$ = O redox potentials (~1.28 V) corresponds to the highest reported oxygen evolution activity. These findings are based on empirical data—oxygen evolution rates and cyclic voltammetry redox couples—absent in prior Sabatier—principle—based works on similar families of catalysts.

2. Results

A schematic representation of the complexes considered in this study are shown in Figure 1. Included in the set of model catalysts are those with neutral and negatively charged ligands. Each catalyst studied may be considered a deviation from another; either by substitution of an R group or similar modification can one catalyst be related to at least one other. This allows for comparisons of the precise effect of the ligand structure on catalytic activity and predictor relationships; these catalysts are chosen to enable both the broad study of the Ru(NNN)(NN), Ru(NNN)(NO), and similarly structured families, as well as more narrow—scoped considerations of electronic structure effects. Table S1 shows the oxygen evolution rates as determined for each of the catalysts studied. These values were obtained at room temperature; see Section 4 for more details. The oxygen evolution rate of the bda—type complexes is not considered for our analysis, as Ru(bda)(4—pic)₂ and Ru(bda)(isoq)₂ have a second—order rate with catalyst concentration [53], unlike the other catalysts studied—first—order with catalyst concentration.

The thirteen catalysts were modelled in each of the seven states of typical WNA mechanisms, outlined in Figure 2. Each geometry was optimized, and free energies of each state were determined for each catalyst; see Section 4 for computational details. The results of the DFT optimization and energy computation are reported in Tables S2–S4: the free energies of each intermediate, computed redox potentials, and changes in free energy of the WNA processes. Table 1 cites the experimentally reported redox potentials alongside computed redox couples for ET and PCET paths. Ru^{III} states are computed in the singlet state, and Ru^{III} and Ru^V intermediates are computed at the doublet state. Ru^{IV} states are primarily triplet as these are found to have lower energy, except for bda—like catalysts, which were singlet. Most of the computed redox potentials are within ~0.2 V of the reported redox couples. This serves to validate the choice of basis set and the use of the generalized gradient approximation methodology, B3LYP, used in this study. Table 1 reports the computational assignment of the specific redox couple at pH = 0 for each catalyst's redox mechanism.

With such a large set of catalysts and species in our data set, we must validate our choice of basis set and computational methodology. Due to systematic error inherent in DFT methods, agreement with experimental redox couples is ideally near/with ~0.2 V agreement, the generally accepted margin of error for computed disagreement using a similar basis set and computational methods [13,42,44,51,54]. However, due to the large number of catalysts and experimental evidence, some computed couples may have slightly larger differences; prominent examples of this include the Ru^{II}/Ru^{III} couple of well—studied Ru(tpy)(bpy) catalysts. It is computationally predicted to advance to Ru^{III}

Catalysts 2022, 12, 863 5 of 15

via a PCET reaction at pH = 0, Table 1; however, experimental ~1.04 V value was shown to correspond to the ET process at pH = 0 [54,55]. Earlier DFT calculations with the inclusion of two explicit water molecules resulted in ~1.06 V Ru^{II}/Ru^{III} ET for Ru(tpy)(bpy) close to observed in experiment [54]. Such variability is, in part, related to difficulties in predicting pKa values which are dependent on the modeling of the solvation environment of the catalyst.

Table 1. Computed Redox potentials (V) for pH = 0 for each of the thirteen catalysts ET as well as PCET paths are considered.

	Ru ^{II} /Ru ^{III}		Ru ^{III} /Ru ^{IV}				Ru ^{IV} /Ru ^V	
	II–H ₂ O/ III–H ₂ O	II–H ₂ O/ III–OH	III–H ₂ O/ IV–OH	$III-H_2O/$ $IV = O$	III–OH/ IV–OH	III-OH/ IV = O	IV-OH/V=O	IV = O/ $V = O$
Ru(EtoTpy)(4pic) ₂	1.30 0.97 V	0.69 [44]	1.26	0.32	1.87	0.94	1.29	2.23
Ru(Tpy)(4pic) ₂	1.38 1.00 V	0.70 [44]	1.42	0.30	2.09	0.97	1.21	2.33
Ru(tpy)(bpy)	1.32 0.75 1.04 V [56]		1.68	0.46 2.26 1.23 V [56], 1.39 V [57]		1.03	1.15 2.37 1.60 V [58], 1.73 V [59], 1.80 V [60]	
Ru(EtoTpy)(bpy)	1.21 0.98 V	0.70 [61]	1.44	0.48 1.24 V	1.95 V [61]	1.00	1.24	2.19
Ru(TpyCl)(QC)	0.68 0.61 V	0.47	1.25	0.75	1.45	0.96	1.30	1.79
Ru(EtoTpy)(QC)	0.59		1.14	0.76 1.19	1.27 V [*]	0.89	1.29 1.73	1.68 V [*]
Ru(Tpy)(QC)	0.62 0.42 0.67 V [62], 0.82 V [*]		1.22	0.75 1.42 1.20 V [62], 1.36 V [*]		0.95	1.28 1.75 1.62 [62], 1.75 V [*]	
Ru(TpyMeO)(bpy)	1.23 No D	1.00 ata	1.48	0.52	1.70	0.74	1.22	2.18
Ru(Tpy-Me)(bpy)	1.26 0.79 No Data		1.50	0.53	1.98	1.00	1.31	2.28
Ru(Tpy-Cl)(bpy)	1.40 No D	0.82 ata	1.56	0.45	2.13	1.02	1.34	2.45
Ru(bda)(isoq) ₂ **	0.19 0.17 ** 0.63 V [5	0.91 3] 1.06	2.08 1.31	1.74 1.09 V	1.36 V [53]	1.02	1.03 1.52 1.27 V	1.38 V [53]
Ru(bda)(4pic) ₂	0.09 0.78 0.66 V [63]		0.98	1.82 0.30 1.15 V [63]		1.13	2.12 1.28 1.35 V [63]	
Ru(tpy)(bpyNO)	1.09 0.79 0.82 V [13]		1.50	0.65 1.79 0.86 V [13]		0.95	1.32	2.16

Experimental redox potentials are located beneath computed redox potentials. "No Data" signifies that no experimentally derived couples have been reported. Values in brackets indicated the reference for experimental data. [*] refers to work pending publication. ** numbers in bold indicate earlier published DFT results with use of five explicit water molecules [51].

Table 1 reports computational assignment of the specific redox couple at pH = 0 for each catalyst's redox mechanism. Differences in the redox mechanism within the catalyst of the (NNN)(NN) structure suggest that specific ligand modifications sufficiently alter the electronic structure to overcome the effect of the inner coordination sphere's influence. For the bda class of catalysts which act via 7–coordinate Ru^{IV} and Ru^{V} intermediates, DFT calculations, without consideration of the structure of intermediates determined experimentally, produce absurd results, Table 1. Computed steps with potentials in the 1.7–2.12 V range are artificially high due to de—coordination of the —COO— ligand. This indicates that the broad, careless application of a computational technique might overlook

Catalysts 2022, 12, 863 6 of 15

promising catalytic systems, if said technique fails to capture the true structures of the intermediates. Thus, the Ru(bda)(isoq)₂ entry in Table 1 was augmented with DFT results from an earlier detailed study which used five explicit water molecules for a more realistic modeling of the catalyst active site [51].

Having validated our choice of basis set and computational methodology, we proceeded with our adaption of conventional LFESR analysis to our set of homogenous, Ru-based catalysts outlined in Figure 1. Following prior methodologies for LFESR analysis [64], we computed energies of the Ru^{III}-OH, Ru^{IV} = O, and Ru^{III}-OOH intermediates (Table S5) relative to the stable Ru^{II} species for each catalyst; these energies relative to the rest state (E_{RRS}) are plotted against the representative parameter of the redox potential of the PCET Ru^{II}-H₂O to Ru^{III}-OH reaction in Figure 3.

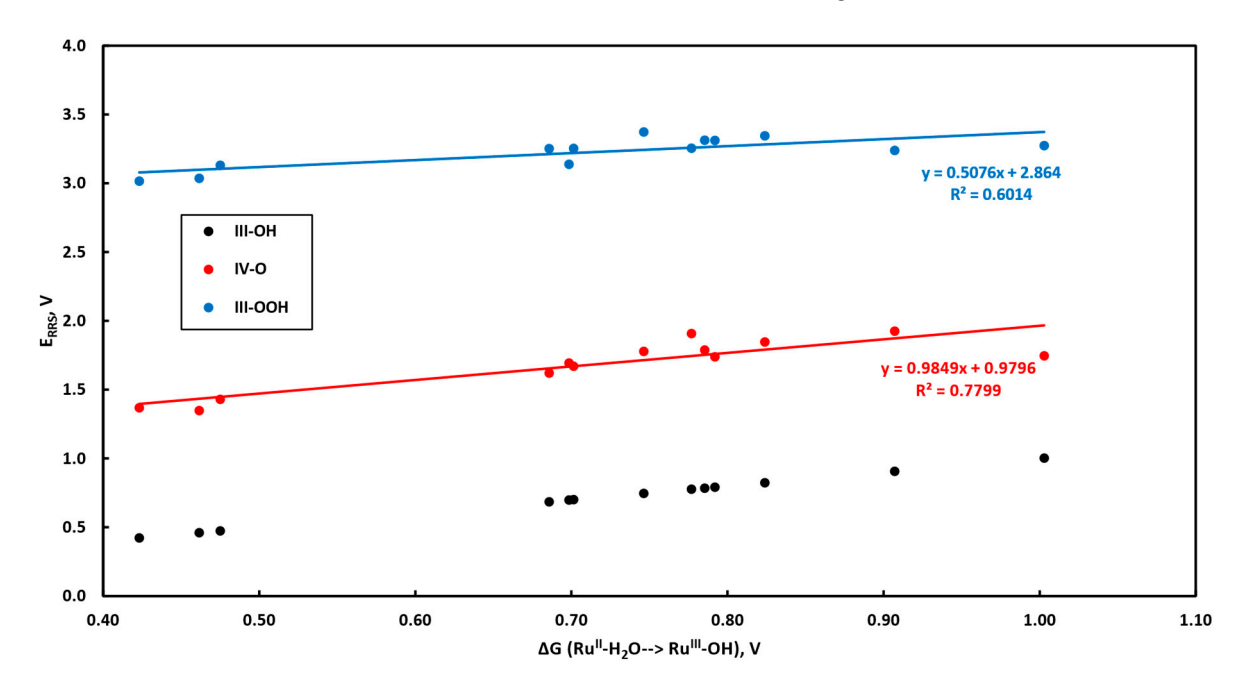


Figure 3. Free—energy scaling relationships for E_{RRS} of Ru^{III} —OH, Ru^{IV} = O, and Ru^{III} —OOH for the thirteen molecular catalysts considered in this study.

Essential in the construction of volcano plots is establishing LFESRs, relating the energetics of different catalytic intermediates onto a single variable [34]. In principle, different intermediates' stabilities are interrelated and cannot be significantly altered independently. Should a set of LFESRs be established for a particular intermediate, mathematical relationships derived therein may describe the entire energetic landscape in terms of a single descriptor; see Methods. Plots of the (negative) change in free energy along the potential—determining step of a mechanism against a "descriptor" variable—for which the existence of LFESRs contains information on each catalyst's entire energetic landscape—indicate "ideal" catalysts; this is a volcano plot [34].

The free—energy scaling relationships between the redox reaction of $Ru^{II}-H_2O$ to $Ru^{III}-OH$ are moderately linear with the E_{RRS} of $Ru^{IV}=O$ but do not have a strong linear relationship with the E_{RRS} of the $Ru^{III}-OOH$ species resulting from WNA on Ru-oxo species (Figure 3). Reports of LFESR—based analysis on catalytic systems often produce volcano plots using regressions with a high value for R^2 , usually above or near 0.90 [64,65]. Few analyses consider LFESR methods below R^2 of 0.8 [66], which we will treat as a cutoff for sufficiently linear correlation. Reselection of the descriptor (x-axis variable in Figure 3) does not result in sufficiently strong correlations required for LFESR analysis; Tables S6 and S7 show the complete set of correlations of each descriptor against each E_{RRS} . Although some descriptors, such as the $Ru^{III}-H_2O$ to $Ru^{IV}-OH$ PCET reaction and the $Ru^{IV}=O$ to $Ru^{V}=O$ ET reaction, correlate well with early stages in the mechanism, they correlate

Catalysts 2022, 12, 863 7 of 15

more poorly with the WNA step. The E_{RRS} for the Ru^{III} –OOH intermediate does not correlate strongly with any descriptor studied (Tables S6 and S7). This step tends to have the weakest correlations with the descriptor variables, and its strongest correlation is with the Ru^{II} – H_2 O PCET step, already dismissed above (Figure 3). As such, these results indicate that this approach to LFESR analysis is inappropriate for the set of catalysts chosen; however, we will continue our study with Sabatier–principle and volcano–plot based analysis using empirical data of oxygen evolution rates—an approach which, to the best of our knowledge, is unpublished.

To continue our analysis, we consider alternative volcano plot/Sabatier—principle—based analysis, using known oxygen evolution rates as an experimentally derived measure of the quality of each catalyst. This approach to analysis continues in parallel with conventional LFESR—based analysis yielding volcano plots, using η_{th} as the sole, theoretical analogue of catalytic effectiveness and quality. Considering, still, the utility for Ru—based WOCs to access the high—valent Ru^V = O intermediate prior to WNA and O—O bond formation, our volcano plot and Sabatier—principle—based analysis in Figure 4 focuses on four late—stage steps along the WNA cycle: (A) Ru^{IV} = O to Ru^V = O, (B) WNA on Ru^V = O (Ru^V = O to Ru^{III}—OOH), (C) Ru^{IV} = O to Ru^{IV}—OH and (D) Ru^{IV}—OH to Ru^V = O.

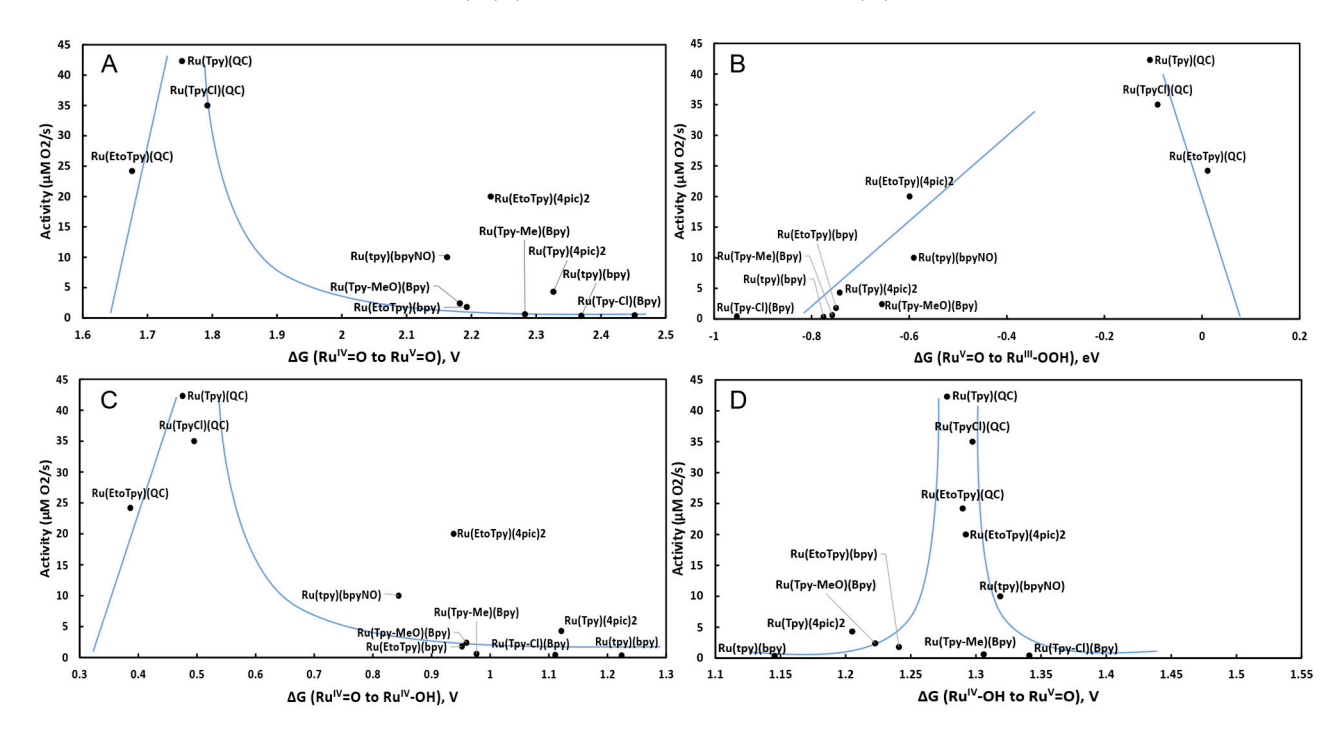


Figure 4. Plots of activity over computed (**A**) potential of conventional $Ru^{IV} = O$ to $Ru^{V} = O$ ET redox reaction, (**B**) change in free energy of WNA on $Ru^{V} = O$, (**C**) change in free energy of the $Ru^{IV} = O$ to $Ru^{IV} - OH$ protonation reaction, and (**D**) redox potential of the PCET $Ru^{IV} - OH$ to $Ru^{V} = O$ reaction. Bda—type catalysts are omitted due to their 2nd—order dependence on catalyst concentration.

Each graph in Figure 4 identifies a region of ideal catalytic activity based on a band of relative energies of intermediates in the WNA mechanism. Figure 4A explores a Sabatier–based relationship between the $Ru^{IV}=O$ to $Ru^V=O$ ET reaction, often cited as needed for O–O bond formation and oxygen evolution activity; easier access to the high–valent Ru^V intermediate suggests high activity in O_2 evolution. Figure 4B supports the necessity of reaching $Ru^V=O$ prior to the WNA reaction allowing for negative ΔG for the O–O bond formation. However, the catalysts with the highest oxygen evolution rates are observed to experience a minimally downhill reaction in forming O–O bonds: $\Delta G \sim > -0.1$ eV. This ensures the minimal overpotential associated with energetic efficiency. One can note similar in the oxygen–evolving complex of photosystem II: the peroxo state within ~ 0.2 eV of the oxidized S_3 state, predicted computationally. [67] Figure 4C suggests

Catalysts 2022, 12, 863 8 of 15

that ideal Ru-based catalysts have only a slightly thermodynamically uphill protonation from Ru^{IV} = O to Ru^{IV} – OH; unsurprisingly, this is similar to what is seen in Figure 4A. It should be noted that the bda family excluded from this analysis has Ru^{IV} – OH state which is thermodynamically more stable than the Ru^{IV} = O state and, thus, was characterized by XRD and NMR [53]. Figure 4D identifies a very narrow range of energies of the PCET Ru^{IV} – OH to Ru^V = O reaction, centered at ~1.28 V, where the four most active catalysts reside, surrounded by lower – activity catalysts; the catalysts with lowest activity are located farthest from this region. This is the strongest Sabatier – like relationship studied here. Energy allocation close to ~1.23 V per redox step ensures the most optimal catalyst. However, typically, energy increases when a system approaches high oxidation states. The above analysis shows that the development of catalysis achieving high oxidation states at moderate potentials is beneficial.

Having considered LFESR and Sabatier-principle-based analysis for relationships with empirical oxygen evolution activity, our last approach attempts to identify linear regressions of various descriptors against oxygen evolution activity. The predictors in this approach consist of parameters specific to the species late in the WNA cycle—Ru^{IV}, Ru^V, and peroxo species. Table S8 reports the correlations of numerous computed descriptor variables against the experimentally reported oxygen evolution activity and the theoretical overpotential of the catalytic system, Equation (6). Tables S9–S13 report the values for each of the parameters reported in Table S8. Charge and spin densities refer to the Mulliken charge and spin densities as calculated by Gaussian 16 [68]. Note that while computation of the Mulliken spin and density populations is highly dependent upon basis set selection [69], the basis set is kept constant in this work. As such, the systematic bias inherent in basis set selection should not impact regression analysis. The four redox potentials/changes in free energies (Ru^{IV} – OH to Ru^{V} = O, Ru^{IV} = O to Ru^{V} = O, Ru^{IV} = O to Ru^{IV} – OH, WNA on Ru^V = O) are discussed in greater depth later, as they suggest a Sabatier—like relationship with activity rather than with a linear-regression-based model. The theoretical overpotential for most catalysts was taken as the very demanding ETs of the Ru^{IV} = O to Ru^V = O reaction proposed by most works. Thus, we consider only the strongest correlated descriptors of the catalytic mechanisms, the charge densities of the atoms most central to the Ru atom in the peroxide Ru^{III} – OOH state. The charge densities on Ru and the adjacent oxygen atom are strongly inversely correlated with oxygen evolution activity and, suitably, with theoretical overpotential. Although some recent work [70,71] has been conducted on using linear-regression-based methods to find suitable correlators with catalytic activity, a substantially greater amount of work uses Sabatier-principle-motivated methods. Since most of the strongest correlators with activity are also discussed at length in the Sabatier-principle-based analysis, said analysis will compose the bulk of the discussion.

3. Discussion

Related to the employment of linear scaling relationships to find correlations and predictors of catalytic activity is the use of volcano plots, themselves rooted in Sabatier's principle, suggesting catalysts should bind water or an oxo group neither too strongly nor too weakly. Volcano plots may predict catalytic performance—via overpotential or other thermodynamic/kinetic considerations—by consideration of a descriptor variable and LFESRs. Herein, this descriptor is related to estimate other intermediates' relative energies. Sufficiently linear relationships may lead to a "volcano" curve identifying predicted catalytic performance, with ideal catalyst candidates at the peak of the curve [17,26,28].

In 2018, Busch et al. [64] demonstrate the use of linear free—energy scaling relationships to assess the viability of solid state and molecular OER catalysts, using a variety DFT—based functionals. The work included, specifically, the use of generalized gradient approximation functionals (GGAs) and meta—GGA functionals. Using eight model catalysts, composed of a corrole ligand or a porphyrin equivalent, centered about a transition metal atom, Busch et al. were able to produce LFESRs among the E_{RRS} of (* represents a transition metal atom) *-OH, *=O, and *-OOH for various levels of theory for these

Catalysts **2022**, 12, 863 9 of 15

model catalysts. From these LFESRs, Busch et al. were able to describe the thermodynamics of the WNA mechanism in relation to the overpotential of the potential—determining step; thus, they were able to determine a minimal systematic overpotential in terms of a representative parameter of these systems—the E_{RRS} energies of *-OH. The work did not consider mechanisms involving the metal center in the formal oxidation state of (V) such as Ru^V or Fe^V intermediates.

We extended this LFESR-based approach to this broader group of catalysts with less ligand symmetry and, by extension, more ligand variability. The E_{RRS} of the Ru^{III}–OH, Ru^{IV} = O, and Ru^{III} – OOH intermediates are plotted against the representative parameter of the redox potential of the PCET Ru^{II} – H₂O to Ru^{III} – OH reaction in Figure 3. These are based on the computationally derived energetics (Tables S3–S5). Regression against the Ru^{ll} PCET redox potential yielded R^2 of 0.78 and 0.60 for the E_{RRS} of $Ru^{IV} = O$ and $Ru^{III} - OOH$ relative to the initial Ru^{II}-H₂O state. Other descriptor variables were considered to determine the existence of any sufficiently robust LFESRs (Tables S6 and S7), using the cutoff of R² near/above 0.80 as a lower bound of correlation. While some modest correlations were discovered, no mechanism could be constructed from pathways adequately linearly correlated against any individual predictor. As such, conventional LFESR analysis against E_{RRS} is inappropriate for a wholly Ru-based system with an even somewhat variable ligand structure. One report which employed such a technique in the past considered ligand structures of exclusively perfluoroporphyrin and corrole ligands centered on a transition metal atom [64]. This suggests that ligand differences are more highly impactful to the energetics of different intermediates; such differences are enough to change the catalytic activity by over two orders of magnitude, from Ru(tpy–Cl)(bpy) to Ru(tpy)(QC) and a 5x difference with substitution of an electron—donating EtO— group in the even more structurally similar Ru(tpy)(4-pic)₂ to Ru(EtOtpy)(4-pic)₂. Ligand modification to include redox active N-oxide ligand to the Ru metal center can greatly increase catalytic performance; the oxygen evolution rate of Ru(tpy)(bpyNO) is $\sim 30 \times$ that of Ru(tpy)(bpy). *In situ* ligand changes under catalytic conditions cannot be excluded for the least active catalysts if ligand modification has a potential to increase the activity [13] such in situ changes will not be captured in the current analysis.

In 2019, Craig et al. [17] expanded upon the groundwork established by Busch et al. prior. Craig and coworkers considered seventeen molecular OER catalysts based on a variety of transition metals (Ru, Ni, Mn, Co, Cu, and Fe); ruthenium acts at the metal center in nine of these seventeen catalysts. They found that unmodified use of conventional scaling relations for heterogeneous systems did not accurately predict the catalytic activity of a set of homogenous catalysts; typical OER-scaling relations addressing the OER for heterogenous systems neglects the ET reaction from Ru^{IV} = O (or the PCET reaction from Ru^{IV}-OH) yielding Ru^V = O prior to WNA and O-O bond formation; Craig et al. briefly explored this by checking the $Ru^{IV} = O$ to $Ru^{V} = O$ descriptor, discovering that approximately half (five of nine) of their Ru-based catalysts—including $Ru(bda)(4-pic)_2$ and $Ru(bda)(isoq)_2$ —undergo ET for this reaction and have η_{th} defined by this potential-limiting step. As mentioned previously, many Ru-based WOCs require access to RuV prior to formation of an O-O bond since WNA processes on RuIV = O tend to be thermodynamically unfavorable. Numerous catalytic reports indicate catalytic systems based on other elements, and are predicted to form O-O bonds via WNA on Metal^{IV} = O species [72–74]. As such, that our work focuses more on high—valent redox and WNA reactions is appropriate given our exclusive focus on the Ru metal center.

Figure 4C shows the relationships between the oxygen–evolving activity and the protonation energy of $Ru^{IV} = O$, often necessary for the formation of the $Ru^{IV} - OH$ needed for PCET to Ru^{V} . Most of the highly active catalysts show a similar trend, where a lower protonation energy to $Ru^{IV} - OH$ relates to higher oxygen–evolving activity. An exception to this trend is the $Ru(EtO-tpy)(4-pic)_2$ catalyst, found at 0.94 eV; similar behavior is observed with the ET step shown in Fiugre 4A. These exceptions to the Sabatier–like trend suggest that catalytic dependence on these processes are not as strong as the other

Catalysts **2022**, 12, 863 10 of 15

relationships tested. Note that the $Ru^{IV} = O(tpy)(4-pic)_2$ intermediate—most structurally like $Ru(EtO-tpy)(4-pic)_2$ —has a higher protonation energy alongside a lower oxygen evolution rate. This Sabatier—like trend is consistent among the Ru(tpy-R)(bpy) family of catalysts. Taken as a whole, these data indicate that should Ru^{IV} —OH be sufficiently accessible, oxygen evolution activity is not inhibited.

Figure 4D indicates that a PCET redox potential of approximately 1.28 V between Ru^{IV}/Ru^V is achievable and ideal for oxygen–evolving activity. This region is surrounded by immediate and steep binding slopes which lead to overly strong or weak catalystsubstrate interactions, decreasing oxygen evolution activity. That Ru(tpy-Cl)(bpy) has a high PCET redox potential for Ru^{IV}/Ru^V is observed in Table S3. This ideal binding region indicates that catalysts of the Ru(NNN)(NN) and similar ligand structures may have facile access to the catalytically active RuV species with a monotonically increasing series of redox potentials: Ru^{II}/Ru^{III} , Ru^{III}/Ru^{IV} , and Ru^{IV}/Ru^{V} . Should the final redox step in this series be a PCET reaction from Ru^{IV} –OH to Ru^{V} = O, then the catalyst is very likely to have a very small overpotential, considering the near 1.23 V energy allocation per redox step. Note that the lower-activity catalyst Ru(tpyMe)(bpy) exists on the finges of this energetic region. This suggests that while some inactive catalysts may exist within this regime, all of the highly active catalysts studied may minimize overpotential via a PCET reaction from RuIV—OH in this energetic range. This energetic advantage may thus be beneficial – though in isolation insufficient – to promote high catalytic activity. Figure 4B shows that oxygen evolution activity may be low if RuV species display significantly downhill WNA reaction, implying inaccessible, higher—energy Ru^V species. This characterizes most of the catalysts studied, except those with the highest catalytic activity—the Ru(tpy-R)(QC) family of catalysts. Ru(EtO-tpy)(4-pic)₂ offers only slightly weaker oxygen evolution activity and can be located partway along this "weakly binding slope" between the high- and low – activity regimes. Simply, in the absence of transition state energy considerations, the most catalytically active complexes have minutely downhill energetics via WNA processes: $\Delta G \sim -0.1 \text{ eV}$, implying a lower-energy, more accessible Ru^V = O intermediate.

4. Materials and Methods

General Information: Chemicals were bought and used "as is" by AK Scientific, TCI America, and Sigma Aldrich. A Q-POD unit (Milli-Q water purification)—Millipore, Billerica, Massachusetts—provided the Type 1, ultrapure water. Resistivity at 25 degrees Celsius was $18.2~\mathrm{M}\Omega\cdot\mathrm{cm}$. Materials obtained from Sigma—Aldrich did not undergo further purification.

Pearson Coefficient: The linear relationship between the two variables on a scatter plot is strongest when the points are closer to lying on a straight line. The Pearson coefficient r quantifies the strength of this linear relationship. For two variables x and y and data taken in n pairs,

$$\{[x_1,y_1], [x_2,y_2], \dots [x_n,y_n]\},$$
 (7)

the Pearson correlation coefficient is given by:

$$R = \frac{\sum_{i=1}^{n} (x_i - \overline{x})(y_i - \overline{y})}{\sqrt{\sum_{i=1}^{n} (x_i - \overline{x})^2 \sum_{i=1}^{n} (y_i - \overline{y})^2}},$$
(8)

where \overline{x} and \overline{y} represent the means of the x and y variables, respectively. The strongest correlations have magnitudes of R closer to 1, and the value of the correlation coefficient is always between -1 and +1. Positive values indicate positive linear relationships; negative values represent negative linear relationships.

 O_2 Evolution: Oxygen evolution was measured with an Oxygraph system from Hansatech Instruments, consisting of a polarographic, Clark—type oxygen electrode. O_2 evolution activity was measured at room temperature. Linear calibration was performed via measurement of O_2 —saturated and depleted levels at room temperature. Sodium dithionite was used to deplete O_2 from water. Water solubility at room temperature is

Catalysts 2022, 12, 863 11 of 15

(262 μ mol/L). The corresponding signal drop was set equal to this water solubility. In catalysis, 500 μ L of catalyst was stirred at 900 rpm in a borosilicate vessel. Conditions were pH = 1, with 0.1 M nitric acid. Oxygen concentration was monitored over time with the addition of 20 mM of sacrificial oxidant, cerium(IV) ammonium nitrate (Ce^{IV}). Oxygen evolution rates are not reported for bda—like catalysts due to their 2nd—order dependence on catalyst concentration, unlike the other 1st—order catalysts.

Linear Free—Energy Scaling Relationships: Linear free—energy scaling relationships (LFESRs) are composed of strongly correlated relationships between free energies of intermediates of the catalytic systems. Such relationships allow one to cast various intermediates' energies relative to rest state (E_{RRS}) in terms of another, single variable or descriptor, such as another intermediate's E_{RRS} or the change in free energy of a key reaction. Such descriptors will later define the volcano plot landscape. LFESRs capture information regarding the electronic effects of a system. An example of a LFESR of some i^{th} intermediate against a descriptor variable resembles the form:

$$E_{RRS}(i) = m_i \times E_{RRS}(descriptor) + b_i$$
 (9)

 m_i and b_i parameterize the scaling relation to the descriptor variable for each intermediate i. Such an approach fails if the correlation between $E_{RRS}(i)$ and $E_{RRS}(descriptor)$ is too weak– $R^2 \sim 0.80$ is a typical cutoff.

Volcano Plots: Volcano plots can be constructed only with the existence of a sufficiently correlated set of LFESRs. Volcano plots demonstrate the relationship of intermediates' free energies or changes in energies in reactions (y-axis) against the stability of a descriptor variable's E_{RRS} (x-axis). The LFESRs define the lines of the volcano plot of the reaction energies. Volcano plots tend to be represented in terms of the potential—determining step or the theoretical overpotential η_{th} (see Equation (6)). Volcano plots tend to have three regions, corresponding to strong binding, weak binding, and the "ideal catalyst" center, as described by the energetics of the descriptor intermediate.

DFT Calculation: The B3LYP methodology was used in all density functional theory (DFT) calculations. Light atoms (O, C, H, N) are computed with the $6-31G^*$ basis set, and heavier atoms (Cl, Ru) are computed with the dgdzvp basis set. The conductor polarized continuum model (CPCM) modelled water solvation for all intermediates and calculations. Redox potentials and changes in free energies are computed at DFT-optimized geometries, with energies of products minus the energies of reactants. In redox processes, 4.44 V accounts for the NHE voltage. -11.64 eV is used to describe change in free energy for H⁺ solvation. Intermediates' energies are first optimized. Single point calculations follow, determining vibrational frequencies and thermal/electronic energies. Quadratic convergence criteria were required to optimize certain intermediates. Implicit consideration of the water molecule in WNA processes was carried out with the free energy of a water molecule computed with 6-31 G* at the B3LYP level of theory.

5. Conclusions

Linear free—energy scaling relationships were used alongside regression—based analysis to predict catalytic performance of homogeneous, single—atom, and solid—state water oxidation catalysts. This study considers thirteen similarly structured, homogenous Ru—based catalysts—some among the most active homogenous catalysts—using the conventional methods of LFESR analysis and finds conventional approaches and descriptors cannot be broadly applied to homogenous catalysts. We report that general LFESR—based methods yield insufficiently robust linear relationships between descriptor variables. We include empirical rates of oxygen evolution in addition to the conventionally reported theoretical overpotentials in our analysis. Our study reveals several Sabatier—principle—like relationships between relative energies of high—valent intermediates against experimental oxygen evolution rates. We observe ideal ranges of relative energies of the Ru $^{\rm IV}={\rm O}$ and Ru $^{\rm IV}-{\rm OH}$ intermediates, as well as ideal changes in free energy of the water nucleophilic attack process on Ru $^{\rm V}={\rm O}$. These narrow ranges are strongly associated with the highest rates

Catalysts **2022**, 12, 863

of oxygen evolution activity and suggest the significance of the Ru^{IV} –OH intermediate, easing access to the high–valent and catalytically competent Ru^{V} = O state.

The data presented support the established understanding of molecular water oxidation catalysis, while providing insight into key energetic ranges corresponding to high levels of oxygen evolution activity. The existence and substitution of electron—donating groups to the ligand backbone of Ru—based WOCs has been demonstrated to lead to high levels of oxygen evolution activity. Such is observed with our results for the $Ru(tpy-R)(4-pic)_2$ catalyst with EtO- group substitution. Similarly, the hypothesized significance of proximal bases to metal—oxo groups is corroborated; the carboxyl groups of QC—type and bda—type catalysts likely lower energetic barriers to O-O bond formation, evidenced by their high rates of oxygen evolution activity. An oxygen atom transfer process to yield a proximal N-oxide group—observed in Ru(tpy)(bpyNO)—may have as much of a 30× increase in catalytic activity. Such structural motifs are mirrored in nature's finest water oxidation catalyst, the oxygen-evolving complex of photosystem II. Newly discovered are precise energetic ranges for promising catalytic rates in Ru-based catalysts. We show that the most highly active catalysts have a minimally downhill reaction in the WNA and O-O bond formation step; similarly, the ET reaction of Ru^{IV} = O to Ru^V = O with potentials near 1.75 V correspond to high oxygen evolution rates. The evidence reported herein suggests the significance of the Ru^{IV} –OH intermediate. With access to the high–valent, catalytically competent Ru^V species critical for high rates of oxygen evolution, the lower-potential PCET pathway from Ru^{IV} – OH—a reaction with a very strong Sabatier – like relationship between oxygen evolution activity and redox potential—inspires further study. We find the strongest Sabatier-like relationship here, with a narrow band of redox potentials, centered near 1.28 V of the Ru^{IV} – OH to Ru^V = O PCET reaction. This suggests that a monotonically increasing series of redox potentials in a redox mechanism may conclude with a Ru^{IV} – OH PCET reaction prior to O – O bond formation, resulting in a catalyst with incredibly low overpotential.

Supplementary Materials: The following supporting information can be downloaded at: https://www.mdpi.com/article/10.3390/catal12080863/s1, Optimized DFT Coordinate File. Supplementary Information File. Table S1: Comparison of O2 evolution rates for structurally similar catalysts; Table S2: Free energies of intermediates computed at the B3LYP level of theory; Table S3: Redox Potentials of the catalysts, computed from free energies at B3LYP level of theory; Table S4: Free energies of reaction of WNA processes; Table S5: Computed E_{RRS} for different intermediates; Table S6. Correlation (R) for each descriptor energy against the set of E_{RRS} ; Table S7. E_{RRS} for each descriptor energy against the set of E_{RRS} ; Table S8. Pearson's coefficients for each of the descriptor variables correlating with oxygen evolution activity and theoretical overpotential E_{RRS} ; Table S9: Energetics relevant to E_{RRS} , E_{RRS} , and peroxide formation correlated to E_{RRS} evolution rate; Table S10: Parameters relevant to the E_{RRS} evolution E_{RRS} and E_{RRS} evolution E_{RRS

Author Contributions: G.B.: writing—original draft preparation; data curation; investigation; methodology. Y.P.: writing—review and editing; supervision, project administration; funding acquisition; conceptualization. All authors have read and agreed to the published version of the manuscript.

Funding: This research was supported by NSF, CHE-1900476 (Y.P.) and by GM132024 (T32 Molecular Biophysics Training Program to G.B.) from the National Institute of General Medical Sciences (NIGMS).

Data Availability Statement: Refer to Supplementary Materials to access data supporting results.

Acknowledgments: We acknowledge Jully Patel for her assistance in preparation and characterization of catalysts Ru(tpyCl)(QC), Ru(EtOtpy)(QC), and Ru(tpy)(QC).

Conflicts of Interest: The authors declare no conflict of interest.

Catalysts **2022**, 12, 863 13 of 15

References

- 1. Lewis, N.S. Research opportunities to advance solar energy utilization. *Science* 2016, 351, aad1920. [CrossRef]
- 2. Gust, D.; Moore, T.A.; Moore, A.L. Solar fuels via artificial photosynthesis. *Acc. Chem. Res.* **2009**, 42, 1890–1898. [CrossRef] [PubMed]
- 3. Song, W.; Chen, Z.; Brennaman, M.K.; Concepcion, J.J.; Patrocinio, A.O.T.; Iha, N.Y.M.; Meyer, T.J. Making solar fuels by artificial photosynthesis. *Pure Appl. Chem.* **2011**, *83*, 749–768. [CrossRef]
- 4. Tachibana, Y.; Vayssieres, L.; Durrant, J.R. Artificial photosynthesis for solar water-splitting. *Nat. Photonics* **2012**, *6*, 511–518. [CrossRef]
- 5. Lewis, N.S.; Nocera, D.G. Powering the planet: Chemical challenges in solar energy utilization. *Proc. Natl. Acad. Sci. USA* **2006**, *103*, 15729–15735. [CrossRef]
- 6. Nocera, D.G. Solar fuels and solar chemicals industry. Acc. Chem. Res. 2017, 50, 616–619. [CrossRef]
- 7. Nocera, D.G. The Artificial Leaf. Acc. Chem. Res. 2012, 45, 767–776. [CrossRef]
- 8. Kim, W.; Edri, E.; Frei, H. Hierarchical inorganic assemblies for artificial photosynthesis. *Acc. Chem. Res.* **2016**, *49*, 1634–1645. [CrossRef]
- 9. Young, K.J.; Martini, L.A.; Milot, R.L.; Snoeberger III, R.C.; Batista, V.S.; Schmuttenmaer, C.A.; Crabtree, R.H.; Brudvig, G.W. Light-driven water oxidation for solar fuels. *Coord. Chem. Rev.* **2012**, *256*, 2503–2520. [CrossRef]
- 10. Karkas, M.D.; Verho, O.; Johnston, E.V.; Åkermark, B. Artificial photosynthesis: Molecular systems for catalytic water oxidation. *Chem. Rev.* **2014**, *114*, 11863–12001. [CrossRef]
- 11. Blakemore, J.D.; Crabtree, R.H.; Brudvig, G.W. Molecular catalysts for water oxidation. *Chem. Rev.* **2015**, *115*, 12974–13005. [CrossRef] [PubMed]
- 12. Sivula, K.; Van De Krol, R. Semiconducting materials for photoelectrochemical energy conversion. *Nat. Rev. Mater.* **2016**, *1*, 15010. [CrossRef]
- 13. Ravari, A.K.; Zhu, G.; Ezhov, R.; Pineda-Galvan, Y.; Page, A.; Weinschenk, W.; Yan, L.; Pushkar, Y. Unraveling the mechanism of catalytic water oxidation via de novo synthesis of reactive intermediate. *J. Am. Chem. Soc.* **2019**, *142*, 884–893. [CrossRef] [PubMed]
- 14. Sheridan, M.V.; Sherman, B.D.; Xie, Y.; Wang, Y. Heterogeneous water oxidation catalysts for molecular anodes and photoanodes. *Sol. RRL* **2021**, *5*, 2000565. [CrossRef]
- 15. Ye, S.; Ding, C.; Liu, M.; Wang, A.; Huang, Q.; Li, C. Water oxidation catalysts for artificial photosynthesis. *Adv. Mater.* **2019**, *31*, 1902069. [CrossRef]
- 16. Thalluri, S.M.; Bai, L.; Lv, C.; Huang, Z.; Hu, X.; Liu, L. Strategies for semiconductor/electrocatalyst coupling toward solar-driven water splitting. *Adv. Sci.* **2020**, *7*, 1902102. [CrossRef]
- 17. Craig, M.J.; Coulter, G.; Dolan, E.; Soriano-López, J.; Mates-Torres, E.; Schmitt, W.; García-Melchor, M. Universal scaling relations for the rational design of molecular water oxidation catalysts with near-zero overpotential. *Nat. Commun.* **2019**, *10*, 4993. [CrossRef]
- 18. Hessels, J.; Detz, R.J.; Koper, M.T.M.; Reek, J.N.H. Rational design rules for molecular water oxidation catalysts based on scaling relationships. *Chem. Eur. J.* **2017**, 23, 16413–16418. [CrossRef]
- 19. Schilling, M.; Böhler, M.; Luber, S. Towards the rational design of the Py5-ligand framework for ruthenium-based water oxidation catalysts. *Dalt. Trans.* **2018**, *47*, 10480–10490. [CrossRef]
- Huang, J.; Zhang, Y.; Ding, Y. Rationally designed/constructed CoO_x/WO₃ anode for efficient photoelectrochemical water oxidation. Acs Catal. 2017, 7, 1841–1845. [CrossRef]
- 21. Gao, J.; Huang, X.; Cai, W.; Wang, Q.; Jia, C.; Liu, B. Rational Design of an Iridium–Tungsten Composite with an Iridium–Rich Surface for Acidic Water Oxidation. *ACS Appl. Mater. Interfaces* **2020**, *12*, 25991–26001. [CrossRef] [PubMed]
- 22. Latimer, A.A.; Kulkarni, A.R.; Aljama, H.; Montoya, J.H.; Yoo, J.S.; Tsai, C.; Abild-Pedersen, F.; Studt, F.; Nørskov, J.K. Understanding trends in C–H bond activation in heterogeneous catalysis. *Nat. Mater.* **2017**, *16*, 225–229. [CrossRef]
- 23. Liao, P.; Getman, R.B.; Snurr, R.Q. Optimizing open iron sites in metal–organic frameworks for ethane oxidation: A first-principles study. *ACS Appl. Mater. Interfaces* **2017**, *9*, 33484–33492. [CrossRef] [PubMed]
- 24. Yang, X.-F.; Wang, A.; Qiao, B.; Li, J.; Liu, J.; Zhang, T. Single-atom catalysts: A new frontier in heterogeneous catalysis. *Acc. Chem. Res.* 2013, 46, 1740–1748. [CrossRef] [PubMed]
- 25. Flytzani-Stephanopoulos, M. Gold atoms stabilized on various supports catalyze the water–gas shift reaction. *Acc. Chem. Res.* **2014**, *47*, 783–792. [CrossRef]
- 26. Abild-Pedersen, F.; Greeley, J.; Studt, F.; Rossmeisl, J.; Munter, T.R.; Moses, P.G.; Skulason, E.; Bligaard, T.; Nørskov, J.K. Scaling properties of adsorption energies for hydrogen-containing molecules on transition-metal surfaces. *Phys. Rev. Lett.* **2007**, *99*, 16105. [CrossRef]
- 27. Nørskov, J.K.; Bligaard, T.; Rossmeisl, J.; Christensen, C.H. Towards the computational design of solid catalysts. *Nat. Chem.* **2009**, *1*, 37–46. [CrossRef]
- 28. Wodrich, M.D.; Sawatlon, B.; Busch, M.; Corminboeuf, C. The genesis of molecular volcano plots. *Acc. Chem. Res.* **2021**, *54*, 1107–1117. [CrossRef]
- 29. Cordova, M.; Wodrich, M.D.; Meyer, B.; Sawatlon, B.; Corminboeuf, C. Data-driven advancement of homogeneous nickel catalyst activity for aryl ether cleavage. *Acs Catal.* **2020**, *10*, 7021–7031. [CrossRef]

Catalysts **2022**, 12, 863 14 of 15

30. Busch, M.; Wodrich, M.D.; Corminboeuf, C. Linear scaling relationships and volcano plots in homogeneous catalysis–revisiting the Suzuki reaction. *Chem. Sci.* **2015**, *6*, 6754–6761. [CrossRef]

- 31. Mori-Sánchez, P.; Cohen, A.J.; Yang, W. Many-electron self-interaction error in approximate density functionals. *J. Chem. Phys.* **2006**, *125*, 201102. [CrossRef] [PubMed]
- 32. Ruzsinszky, A.; Perdew, J.P.; Csonka, G.I.; Vydrov, O.A.; Scuseria, G.E. Density functionals that are one-and two-are not always many-electron self-interaction-free, as shown for H₂⁺, He₂⁺, LiH⁺, and Ne₂⁺. *J. Chem. Phys.* **2007**, *126*, 104102. [CrossRef] [PubMed]
- 33. Haunschild, R.; Henderson, T.M.; Jimenez-Hoyos, C.A.; Scuseria, G.E. Many-electron self-interaction and spin polarization errors in local hybrid density functionals. *J. Chem. Phys.* **2010**, *133*, 134116. [CrossRef] [PubMed]
- 34. Wodrich, M.D.; Busch, M.; Corminboeuf, C. Accessing and predicting the kinetic profiles of homogeneous catalysts from volcano plots. *Chem. Sci.* **2016**, *7*, 5723–5735. [CrossRef] [PubMed]
- 35. Craig, M.J.; García-Melchor, M. High-throughput screening and rational design to drive discovery in molecular water oxidation catalysis. *Cell Rep. Phys. Sci.* **2021**, *2*, 100492. [CrossRef]
- 36. Galán-Mascarós, J.R. Water oxidation at electrodes modified with earth-abundant transition-metal catalysts. *ChemElectroChem* **2015**, *2*, 37–50. [CrossRef]
- 37. Smith, P.F.; Kaplan, C.; Sheats, J.E.; Robinson, D.M.; McCool, N.S.; Mezle, N.; Dismukes, G.C. What determines catalyst functionality in molecular water oxidation? dependence on ligands and metal nuclearity in cobalt clusters. *Inorg. Chem.* **2014**, 53, 2113–2121. [CrossRef]
- 38. Kamdar, J.M.; Grotjahn, D.B. An overview of significant achievements in ruthenium-based molecular water oxidation catalysis. *Molecules* **2019**, 24, 494. [CrossRef]
- 39. Matheu, R.; Garrido-Barros, P.; Gil-Sepulcre, M.; Ertem, M.Z.; Sala, X.; Gimbert-Suriñach, C.; Llobet, A. The development of molecular water oxidation catalysts. *Nat. Rev. Chem.* **2019**, *3*, 331–341. [CrossRef]
- 40. Zeng, Q.; Lewis, F.W.; Harwood, L.M.; Hartl, F. Role of ligands in catalytic water oxidation by mononuclear ruthenium complexes. *Coord. Chem. Rev.* **2015**, *304*, 88–101. [CrossRef]
- 41. Moonshiram, D.; Alperovich, I.; Concepcion, J.J.; Meyer, T.J.; Pushkar, Y. Experimental demonstration of radicaloid character in a RuV= O intermediate in catalytic water oxidation. *Proc. Natl. Acad. Sci.USA* **2013**, *110*, 3765–3770. [CrossRef] [PubMed]
- 42. Moonshiram, D.; Pineda-Galvan, Y.; Erdman, D.; Palenik, M.; Zong, R.; Thummel, R.; Pushkar, Y. Uncovering the Role of Oxygen Atom Transfer in Ru-Based Catalytic Water Oxidation. *J. Am. Chem. Soc.* **2016**, *138*, 15605–15616. [CrossRef] [PubMed]
- 43. Ertem, M.Z.; Concepcion, J.J. Oxygen Atom Transfer as an Alternative Pathway for Oxygen–Oxygen Bond Formation. *Inorg. Chem.* **2020**, *59*, 5966–5974. [CrossRef]
- 44. Patel, J.; Bury, G.; Ravari, A.K.; Ezhov, R.; Pushkar, Y. Systematic Influence of Electronic Modification of Ligands on the Catalytic Rate of Water Oxidation by a Single-Site Ru-Based Catalyst. *ChemSusChem* **2022**, *15*, e202101657. [CrossRef] [PubMed]
- 45. Erdman, D.; Pineda-Galvan, Y.; Pushkar, Y. Mechanistic analysis of water oxidation catalyst cis-[Ru(bpy)₂(H₂O)₂]²⁺: Effect of dimerization. *Catalysts* **2017**, *7*, 39. [CrossRef]
- 46. Ezhov, R.; Karbakhsh Ravari, A.; Page, A.; Pushkar, Y. Water oxidation catalyst cis-[Ru (bpy)(5,5'-dcbpy)(H₂O)₂]²⁺ and Its Stabilization in Metal–Organic Framework. *ACS Catal.* **2020**, *10*, 5299–5308. [CrossRef]
- 47. Bucci, A.; Menendez Rodriguez, G.; Bellachioma, G.; Zuccaccia, C.; Poater, A.; Cavallo, L.; Macchioni, A. An alternative reaction pathway for iridium-catalyzed water oxidation driven by cerium ammonium nitrate (can). ACS Catal. 2016, 6, 4559–4563. [CrossRef]
- 48. Dengel, A.C.; Griffith, W.P. Studies on transition-metal oxo and nitrido complexes. 12. Synthesis, spectroscopic properties, and reactions of stable ruthenium (V) and osmium (V) oxo complexes containing. alpha.-hydroxy carboxylate and. alpha.-amino carboxylate ligands. *Inorg. Chem.* 1991, 30, 869–871. [CrossRef]
- 49. Planas, N.; Vigara, L.; Cady, C.; Miró, P.; Huang, P.; Hammarstrom, L.; Styring, S.; Leidel, N.; Dau, H.; Haumann, M. Electronic structure of oxidized complexes derived from cis-[Ru^{II} (bpy)₂(H₂O)₂]²⁺ and its photoisomerization mechanism. *Inorg. Chem.* **2011**, *50*, 11134–11142. [CrossRef]
- 50. Pineda-Galvan, Y.; Ravari, A.K.; Shmakov, S.; Lifshits, L.; Kaveevivitchai, N.; Thummel, R.; Pushkar, Y. Detection of the site protected 7-coordinate RuV= O species and its chemical reactivity to enable catalytic water oxidation. *J. Catal.* **2019**, 375, 1–7. [CrossRef]
- 51. Lebedev, D.; Pineda-Galvan, Y.; Tokimaru, Y.; Fedorov, A.; Kaeffer, N.; Copéret, C.; Pushkar, Y. The Key RuV=O Intermediate of Site-Isolated Mononuclear Water Oxidation Catalyst Detected by in Situ X-ray Absorption Spectroscopy. *J. Am. Chem. Soc.* **2018**, *140*, 451–458. [CrossRef] [PubMed]
- 52. Levin, N.; Casadevall, C.; Cutsail III, G.E.; Lloret-Fillol, J.; DeBeer, S.; Rüdiger, O. XAS and EPR in situ observation of Ru (V) oxo intermediate in a Ru water oxidation complex. *ChemElectroChem* **2022**, *9*, e202101271. [PubMed]
- 53. Duan, L.; Bozoglian, F.; Mandal, S.; Stewart, B.; Privalov, T.; Llobet, A.; Sun, L. A molecular ruthenium catalyst with water-oxidation activity comparable to that of photosystem II. *Nat. Chem.* **2012**, *4*, 418–423. [CrossRef] [PubMed]
- 54. Pushkar, Y.; Moonshiram, D.; Purohit, V.; Yan, L.; Alperovich, I. Spectroscopic Analysis of Catalytic Water Oxidation by [Ru^{II}(bpy)(tpy) H₂O]²⁺ Suggests That Ruv O Is Not a Rate-Limiting Intermediate. *J. Am. Chem. Soc.* **2014**, *136*, 11938–11945. [CrossRef]

Catalysts **2022**, 12, 863 15 of 15

55. Jurss, J.W.; Concepcion, J.C.; Norris, M.R.; Templeton, J.L.; Meyer, T.J. Surface catalysis of water oxidation by the blue ruthenium dimer. *Inorg. Chem.* **2010**, *49*, 3980–3982. [CrossRef]

- 56. Wasylenko, D.J.; Ganesamoorthy, C.; Henderson, M.A.; Koivisto, B.D.; Osthoff, H.D.; Berlinguette, C.P. Electronic modification of the [RuII (tpy)(bpy)(OH₂)]²⁺ scaffold: Effects on catalytic water oxidation. *J. Am. Chem. Soc.* **2010**, 132, 16094–16106. [CrossRef]
- 57. Takeuchi, K.J.; Thompson, M.S.; Pipes, D.W.; Meyer, T.J. Redox and spectral properties of monooxo polypyridyl complexes of ruthenium and osmium in aqueous media. *Inorg. Chem.* **1984**, *23*, 1845–1851. [CrossRef]
- 58. Concepcion, J.J.; Jurss, J.W.; Norris, M.R.; Chen, Z.; Templeton, J.L.; Meyer, T.J. Catalytic water oxidation by single-site ruthenium catalysts. *Inorg. Chem.* **2010**, *49*, 1277–1279. [CrossRef]
- 59. Wasylenko, D.J.; Ganesamoorthy, C.; Koivisto, B.D.; Henderson, M.A.; Berlinguette, C.P. Insight into water oxidation by mononuclear polypyridyl Ru catalysts. *Inorg. Chem.* **2010**, *49*, 2202–2209. [CrossRef]
- 60. Wasylenko, D.J.; Ganesamoorthy, C.; Henderson, M.A.; Berlinguette, C.P. Unraveling the roles of the acid medium, experimental probes, and terminal oxidant, (NH₄)₂[Ce(NO₃)₆], in the study of a homogeneous water oxidation catalyst. *Inorg. Chem.* **2011**, *50*, 3662–3672. [CrossRef]
- 61. Yagi, M.; Tajima, S.; Komi, M.; Yamazaki, H. Highly active and tunable catalysts for O 2 evolution from water based on mononuclear ruthenium (II) monoaquo complexes. *Dalt. Trans.* **2011**, *40*, 3802–3804. [CrossRef]
- 62. Hoque, M.A.; Chowdhury, A.D.; Maji, S.; Benet-Buchholz, J.; Ertem, M.Z.; Gimbert-Suriñach, C.; Lahiri, G.K.; Llobet, A. Synthesis, characterization, and water oxidation activity of isomeric Ru complexes. *Inorg. Chem.* **2021**, *60*, 5791–5803. [CrossRef]
- 63. Timmer, B.J.J.; Kravchenko, O.; Liu, T.; Zhang, B.; Sun, L. Off-Set Interactions of Ruthenium–bda Type Catalysts for Promoting Water-Splitting Performance. *Angew. Chem.* **2021**, *133*, 14625–14632. [CrossRef]
- 64. Busch, M.; Fabrizio, A.; Luber, S.; Hutter, J.; Corminboeuf, C. Exploring the limitation of molecular water oxidation catalysts. *J. Phys. Chem. C* **2018**, 122, 12404–12412. [CrossRef]
- 65. Xu, X.; Xu, H.; Cheng, D. Design of high-performance MoS 2 edge supported single-metal atom bifunctional catalysts for overall water splitting via a simple equation. *Nanoscale* **2019**, *11*, 20228–20237. [CrossRef]
- 66. Piqué, O.; Illas, F.; Calle-Vallejo, F. Designing water splitting catalysts using rules of thumb: Advantages, dangers and alternatives. *Phys. Chem. Phys.* **2020**, 22, 6797–6803. [CrossRef]
- 67. Pushkar, Y.; Davis, K.M.; Palenik, M.C. Model of the oxygen evolving complex which is highly predisposed to O–O bond formation. *J. Phys. Chem. Lett.* **2018**, *9*, 3525–3531. [CrossRef]
- 68. Frisch, M.J.; Trucks, G.W.; Schlegel, H.B.; Scuseria, G.E.; Robb, M.A.; Cheeseman, J.R.; Scalmani, G.; Barone, V.; Petersson, G.A.; Nakatsuji, H. *Gaussian 16*; Gaussian, Inc.: Wallingford, CT, USA, 2016.
- 69. Govindasamy, P.; Gunasekaran, S.; Srinivasan, S. Molecular geometry, conformational, vibrational spectroscopic, molecular orbital and Mulliken charge analysis of 2-acetoxybenzoic acid. *Spectrochim. Acta Part A Mol. Biomol. Spectrosc.* **2014**, *130*, 329–336. [CrossRef]
- 70. Du, X.; Zhang, X.; Yang, Z.; Gong, Y. Water oxidation catalysis beginning with CuCo₂S₄: Investigation of the true electrochemically driven catalyst. *Chem. Asian J.* **2018**, *13*, 266–270. [CrossRef]
- 71. Shi, J.; Guo, Y.; Xie, F.; Chen, Q.; Zhang, M. Redox-Active Ligand Assisted Catalytic Water Oxidation by a RuIV= O Intermediate. Angew. Chem. 2020, 132, 4029–4037. [CrossRef]
- 72. Ezhov, R.; Ravari, A.; Bury, G.; Smith, P.; Pushkar, Y. Formation of CoIV=O intermediate at the Boundary of the "Oxo-wall" Induces Water Oxidation. *Res. Sq.* **2020**, 1–21. [CrossRef]
- 73. Siegbahn, P.E.M. Theoretical studies of O-O bond formation in photosystem II. *Inorg. Chem.* 2008, 47, 1779–1786. [CrossRef]
- 74. Coggins, M.K.; Zhang, M.; Chen, Z.; Song, N.; Meyer, T.J. Single-Site Copper (II) Water Oxidation Electrocatalysis: Rate Enhancements with HPO4²⁻ as a Proton Acceptor at pH 8. *Angew. Chem. Int. Ed.* **2014**, 53, 12226–12230. [CrossRef]